

Forces on alkali Rydberg atoms due to non-linearly polarized light

A. Bhowmik* and D. Blume†

Homer L. Dodge Department of Physics and Astronomy,

The University of Oklahoma, Norman, Oklahoma 73019, USA and

Center for Quantum Research and Technology, The University of Oklahoma, Norman, Oklahoma 73019, USA

(Dated: May 5, 2025)

Trapped Rydberg atoms are highly promising candidates for quantum science experiments. While several approaches have been put forward to exert (trapping) forces on isolated Rydberg atoms, a widely applicable lossless technique is lacking. This paper proposes a robust versatile alternative technique that avoids lifetime compromising losses. Our proposal leverages the vector polarizability, which is induced by non-linearly polarized light and is shown to be several orders of magnitude larger than the usual scalar and tensor polarizabilities for commonly used alkali Rydberg series such as the nS , nP , and nD series with principal quantum number n as low as 30. The resulting force can be used to trap isolated Rydberg atoms over long times, which constitutes a key advance that is expected to impact quantum simulation applications, as well as to generate large light-Rydberg-atom hybrid states, which possess non-trivial position-dependent forces.

I. INTRODUCTION

Light-matter interactions play a pivotal role in fundamental research and a wide range of applications. Examples include remarkable developments in quantum optics [1–4], quantum simulations [5–7], quantum information protocols [8], quantum computing [9], quantum sensing [10], high-precision spectroscopy [11], precision measurement of fundamental constants [12], and molecular physics [13].

Electromagnetic fields fundamentally alter the optical properties of materials [14] and are nowadays routinely used to trap cold atoms [15, 16] as well as microparticles [17, 18] and microspheres [19]. This work considers the force on an atom with a high principal quantum number n , specifically an alkali Rydberg atom, in the presence of an external electromagnetic field. Quite generally, the force introduced by the external field is commonly expressed in terms of the dynamic electric dipole polarizability tensor with elements $\alpha_{jk}(\omega)$, where ω denotes the angular frequency of the electromagnetic field ($j, k = x, y$, and z). The application of an electromagnetic field along the x -direction, e.g., produces a polarization vector with x -, y -, and z -components, with the response being quantified by $\alpha_{xx}(\omega)$, $\alpha_{yx}(\omega)$, and $\alpha_{zx}(\omega)$. The dependence of the polarizability tensor on ω provides an exquisite tuning knob that underlies a variety of enabling tools, including magic wavelength-based traps and state-dependent optical lattices for low-lying atomic states [20–24]. In Rydberg atoms, an external electromagnetic field additionally introduces a so-called ponderomotive force, which is associated with the “quiver motion” of the outermost electron [25]. Considering far off-resonant linearly polarized light, earlier work showed that the ponderomotive force dominates over

the polarizability-dependent force, i.e., the polarizability-dependent Stark shift or light shift have been shown to play a secondary role in Rydberg atoms [26–29]. This work identifies a regime where the light shift, which is tunable, dominates over the energy shift due to the ponderomotive force.

Instead of expressing the light shift in terms of the components of the polarizability tensor, it is more convenient to use a decomposition into the scalar polarizability $\alpha^S(\omega)$ (rank-0 tensor), the vector polarizability $\alpha^V(\omega)$ (rank-1 tensor), and the tensor polarizability $\alpha^T(\omega)$ (rank-2 tensor) [30–32]. The effect of the vector and tensor contributions depends on the experimental geometry, i.e., the orientation of the polarization vector and the propagation vector of the light relative to the quantization axis. As a result, the light shift may exhibit a high degree of tunability, offering flexibility through appropriate adjustments of the experimental geometry. Independent tunability of the vector and tensor parts has, e.g., been demonstrated for lanthanide atoms in the ground state [33, 34]. For alkali atoms, in contrast, the vector polarizability tends to be small for the ground state [35], thereby appreciably restricting the tunability; note, though, that tunability of low-lying excited alkali states and alkaline earth metal states via $\alpha^V(\omega)$ has been demonstrated [35–37].

Focusing on linearly polarized light, for which the vector contribution vanishes identically and the polarizability away from resonances scales as $-e^2/(m_e\omega^2)$ [38, 39] [here, e and m_e denote the electron charge and electron mass, respectively], three distinct strategies have been proposed, namely working with (i) blue-detuned light near an atomic resonance [40–42], (ii) blue-detuned bottle beam optical traps that utilize the interference of two Gaussian beams with different beam waists [26], and (iii) beam profiles that exhibit a non-trivial spatial dependence such as optical lattices [43] or Laguerre-Gauss beams [24, 44, 45]. Even though a very recent study [41] predicted that certain Rydberg series—such as, e.g., the $D_{3/2}$ and $D_{5/2}$ series of cesium—feature unexpectedly

* anal.bhowmik-1@ou.edu

† doerte.blume-1@ou.edu

large detunings and, correspondingly, unexpectedly low losses, strategy (i) does not provide a one-fits-all solution. Similarly, strategies (ii) and (iii) have shortcomings [39], that have—up to now—limited their use to niche applications.

This work proposes a versatile alternative strategy, namely the use of elliptically polarized light to exert a force on an alkali Rydberg atom in the direction of the high intensity region of the intensity profile of, e.g., a Gaussian beam. The approach leads to spatially dependent (trapping) forces for various alkali Rydberg series away from resonances, i.e., without introducing lifetime compromising losses. Since the force exerted has contributions from the scalar and tensor parts, which scale as ω^{-2} , as well as the vector part, which scales as ω^{-1} , the proposed strategy allows for the realization of forces that depend comparatively weakly on the wavelength of the light. It is shown that there exists a fairly broad range of experimentally accessible parameters, where the light shift dominates over the energy shift generated by the ponderomotive force. The proposed strategy works for alkali Rydberg atoms of varying size, including n values as low as 30. This feature distinguishes the proposed strategy from a recent alternative approach, which only works for ultra-large Rydberg atoms for which the outer electron is, on average, so far away from the ionic core that it resides in the region where the Gaussian beam has vanishingly small intensity such that the ionic core is trapped via the scalar polarizability and the outer electron hangs on to the core [39].

The remainder of this paper is organized as follows. Section II reviews the theoretical framework employed in this work. Section III presents our results, focusing primarily on rubidium. Finally, Sec. IV summarizes. Technical details as well as calculations for cesium are relegated to several appendices.

II. THEORETICAL FRAMEWORK

We start by discussing the energy shift $U_{\text{gr}}(X, Y, Z, \omega)$ that a ground state atom experiences in the presence of a non-resonant laser with frequency ω . The potential experienced by a ground state atom with single outer or “active” electron is given by the second-order Stark shift $U_{\text{stark}}(X, Y, Z, \omega)$ [30–32],

$$U_{\text{gr}}(X, Y, Z, \omega) = U_{\text{stark}}(X, Y, Z, \omega), \quad (1)$$

where

$$U_{\text{stark}}(X, Y, Z, \omega) = -\frac{I(X, Y, Z)}{2\epsilon_0 c} \left[\alpha^S(\omega) + f^V(A, \theta_k, J, M_J) \alpha^V(\omega) + f^T(\theta_p, J, M_J) \alpha^T(\omega) \right]. \quad (2)$$

In Eq. (2), $I(X, Y, Z, \omega)$ denotes the spatially varying intensity of the laser at the position (X, Y, Z) of the atom, ϵ_0 the vacuum permittivity, and c the speed of

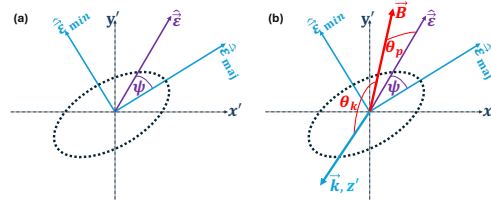


FIG. 1. “Geometric arrangement.” (a) The polarization ellipse (dotted line) lies in the $x'y'$ -plane. $\hat{\epsilon}$, $\hat{\epsilon}_{\text{maj}}$, and $\hat{\epsilon}_{\text{min}}$ denote the polarization vector, major axis, and minor axis, respectively; A is given by the angle ψ , $A = \sin(2\psi)$. (b) The propagation vector \vec{k} , which lies along the z' -axis, is orthogonal to $\hat{\epsilon}_{\text{maj}}$ and $\hat{\epsilon}_{\text{min}}$. The angles θ_k and θ_p define the orientation of \vec{k} and $\hat{\epsilon}$ relative to the external magnetic field vector \vec{B} .

light in vacuum. Explicit expressions for the polarizabilities $\alpha^S(\omega)$, $\alpha^V(\omega)$, and $\alpha^T(\omega)$ are provided in Refs. [32, 46, 47] and not reproduced here. Since we will be working away from resonances, our focus is on the real parts of the polarizabilities, which can be calculated by setting the lifetimes of the intermediate states to zero. Correspondingly, $\alpha^S(\omega)$ denotes the real part of the scalar polarizability and similarly for the vector, tensor, and total polarizabilities. To determine the dynamic scalar, vector, and tensor polarizabilities, we employ the sum-over-states approach [31].

The prefactors $f^V(A, \theta_k, J, M_J)$ and $f^T(\theta_p, J, M_J)$ are coefficients that depend on the total orbital angular momentum quantum number J of the electron and its associated projection quantum number M_J . The quantity A denotes the degree of ellipticity [47]; $A = 0$ and $A = \pm 1$ correspond, respectively, to linearly and circularly polarized light. The angles θ_k and θ_p (Fig. 1) are defined through $\cos \theta_k = \hat{k} \cdot \hat{B}$ and $\cos^2 \theta_p = |\hat{\epsilon} \cdot \hat{B}|^2$, respectively, where \vec{k} denotes the propagation vector, \vec{B} the external magnetic field vector (\vec{B} sets the quantization axis), and $\hat{\epsilon}$ the polarization vector ($\hat{k} = i\hat{\epsilon}^* \times \hat{\epsilon}$). The explicit forms of f^V and f^T read [32, 47]

$$f^V(A, \theta_k, J, M_J) = A \cos \theta_k \frac{M_J}{2J} \quad (3)$$

and

$$f^T(\theta_p, J, M_J) = \frac{3 \cos^2 \theta_p - 1}{2} \frac{3M_J^2 - J(J+1)}{J(2J-1)}. \quad (4)$$

To streamline the discussion to come, we refer to $A \cos \theta_k$ and $(3 \cos^2 \theta_p - 1)/2$ as “geometric factors.” This naming scheme is motivated by the fact that their values are controlled by the relative orientation of the external magnetic field vector and the vectors that characterize the electromagnetic field (Fig. 1). The former geometric factor can take values between -1 and 1 while the latter geometric factor can take values between $-1/2$ and 1 .

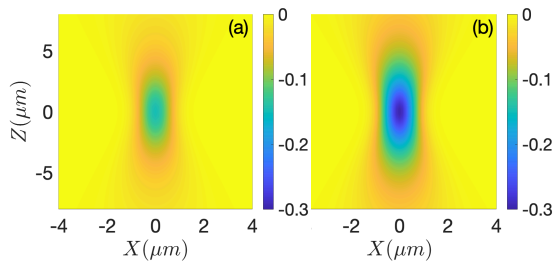


FIG. 2. Trapping potential $U_{\text{gr}}(X, 0, Z, \omega)$ as functions of X and Z for the ground state of rubidium for $\lambda = 1,000$ nm, $\alpha(\omega) = 820.2$ a.u., and $w_0 = 1$ μm . The laser power P of the Gaussian beam is (a) 1.25 mW and (b) 2.5 mW. The color bars indicate the values of $U_{\text{gr}}(X, 0, Z, \omega)$ in mK.

For alkali atoms in the ground state (S state), the spherical symmetry of the electronic wavefunction implies that the tensor polarizability vanishes, i.e., $\alpha^T(\omega) = 0$. Additionally, the vector polarizability contribution in the ground state is typically small [35]. As a result, the combined effect of the vector polarizability and the associated prefactor $f^V(A, \theta_k, J, M_J)$ provides very small tunability of the total dynamic polarizability [35]. Therefore, the trapping potential experienced by an alkali atom in the ground state is essentially independent of the geometric factor $A \cos \theta_k$. As an example, Fig. 2 shows the trapping potential $U_{\text{gr}}(X, 0, Z, \omega)$ for the ground state of the rubidium atom for a Gaussian laser that is characterized by the following intensity pattern:

$$I(X, Y, Z, \omega) = I_0 \frac{1}{1 + \left(\frac{\lambda Z}{\pi w_0^2}\right)^2} e^{-\frac{2(x^2 + y^2)}{w_0^2 \left[1 + \left(\frac{\lambda Z}{\pi w_0^2}\right)^2\right]}}. \quad (5)$$

In Eq. (5), w_0 denotes the beam waist, λ the wavelength of the laser, and I_0 the magnitude of the peak intensity, $I_0 = 2P/(\pi w_0^2)$ (P is the power of the laser). Figure 2 uses typical experimental parameters, namely $w_0 = 1$ μm , $\lambda = 1,000$ nm, and $P = 1.25$ mW and 2.5 mW. For this wavelength, we find that the polarizability $\alpha(\omega)$ of the ground state is equal to 820.2 a.u..

If the size \bar{r} of the Rydberg atom is comparable to or larger than the beam waist w_0 , then the energy shift induced by the electromagnetic field contains, in addition to the Stark shift, a diamagnetic term [25]. In fact, the diamagnetic term has been previously found to be the dominant contribution for linearly polarized light [26–29]. To quantify the size of the Rydberg atom, Fig. 3 shows the probability distribution $r^2 |\Psi_{n_{\text{eff}}, L, J, M_J}^{(0)}(x, y, z)|^2$ of the rubidium Rydberg electron as functions of x and z for $y = 0$, where $r^2 = x^2 + y^2 + z^2$ (x , y , and z denote the Cartesian coordinates of the position vector \vec{r} of the Rydberg electron measured relative to the center-of-mass of the atom). n_{eff} is the effective principal quantum number, see Appendix A. The unperturbed wave functions $\Psi_{n_{\text{eff}}, L, J, M_J}^{(0)}(\vec{r})$, which are calculated in

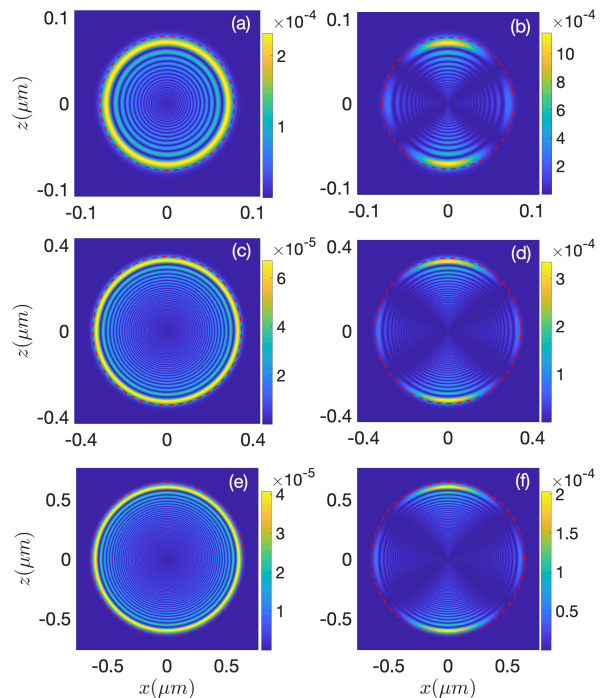


FIG. 3. Probability distribution $r^2 |\Psi_{n_{\text{eff}}, L, J, M_J}^{(0)}(x, 0, z)|^2$ of various rubidium Rydberg states as functions of x and z for $y = 0$. The Rydberg states are (a) $30S_{1/2, +1/2}$, (b) $30D_{3/2, -3/2}$, (c) $60S_{1/2, +1/2}$, (d) $60D_{3/2, -3/2}$, (e) $80S_{1/2, +1/2}$, and (f) $80D_{3/2, -3/2}$. The color bars indicate the values of $r^2 |\Psi_{n_{\text{eff}}, L, J, M_J}^{(0)}(x, 0, z)|^2$ in $(\mu\text{m})^{-1}$. The red dashed lines show the (x_*, z_*) values for which 95% of the $y = 0$ probability of the Rydberg electron lies inside.

the absence of an external field, are normalized such that $\int |\Psi_{n_{\text{eff}}, L, J, M_J}^{(0)}(\vec{r})|^2 d\vec{r} = 1$. Figure 3 shows probability distributions for S -states ($nL_{J, M_J} = nS_{1/2, +1/2}$, left column) and D -states ($nD_{3/2, -3/2}$, right column); throughout, the Rydberg states are labeled by the principal quantum number n , the orbital angular momentum quantum number L , the total angular momentum quantum number J of the electron, and the associated projection quantum number M_J . From top to bottom, n increases from $n = 30$ to 60 to 80. The red dashed lines demarcate the (x_*, z_*) values at which the probability of the Rydberg electron for $y = 0$ has reached 95%. While the $n = 30$ Rydberg state is small compared to typical beam waists, the size of the $n = 60$ and 80 states approaches w_0 .

Accounting for the diamagnetic term, which originates from the square of the vector potential of the oscillating electric field of the far off-resonant laser [25], the Rydberg atom experiences both the Stark shift [see Eq. (2)] and the ponderomotive potential $U_{\text{pon}}(X, Y, Z, \omega)$ [25–29, 48],

$$U_{\text{Ryd}}(X, Y, Z, \omega) = U_{\text{stark}}(X, Y, Z, \omega) + U_{\text{pon}}(X, Y, Z, \omega). \quad (6)$$

It is important to note that the polarizabilities that enter into the Stark shift depend on the state under consideration. For the Rydberg states we employ, just as

for the ground states, the sum-over-states approach [31]. Reference [41] carefully benchmarked our implementation for cesium. Additional benchmarks are presented in Appendix A. Earlier work [41] showed that the polarizabilities of Rydberg states are essentially unchanged, for linearly polarized light, when one transforms from the (J, M_J, I_N, M_I) to the (F, M_F, J, I_N) basis, where I_N denotes the nuclear spin, M_I the associated projection quantum number, F the total angular momentum quantum number of the atom, and M_F its associated projection quantum number. We have verified that the same holds for non-linearly polarized light considered in this work. Consequently, this work uses the (J, M_J, I_N, M_I) basis.

The ponderomotive potential is calculated using first-order perturbation theory. For a Rydberg atom with unperturbed state $\Psi_{n_{\text{eff}}, L, J, M_J}^{(0)}(\vec{r})$, the ponderomotive potential reads [25]

$$U_{\text{pon}}(X, Y, Z, \omega) = \frac{e^2}{2\epsilon_0 c m_e \omega^2} \int d^3 r I(\vec{R} + \vec{r}) |\psi_{n_{\text{eff}}, L, J, M_J}^{(0)}(\vec{r})|^2, \quad (7)$$

where \vec{R} denotes the center-of-mass vector of the atom and \vec{r} the position vector of the Rydberg electron relative to the center of mass of the atom. The next section shows that $U_{\text{pon}}(X, Y, Z, \omega)$ varies slowly compared to the highly oscillatory density of the Rydberg electron. It is important to note that the ponderomotive potential is independent of the geometric factor, i.e., it is the same for linearly and non-linearly polarized light. It can be read off Eq. (7) that the ponderomotive potential is repulsive.

Equation (6) shows that the energy shift that the Rydberg atom experiences is spatially dependent and governed by an interplay between the Stark shift and the ponderomotive potential. The next section demonstrates that far off-resonant, non-linearly polarized laser light, i.e., light with $A \neq 0$, can lead—owing to the induced vector polarizability—to a highly-tunable $U_{\text{stark}}(X, Y, Z, \omega)$. Importantly, this is distinct from the ground-state manifold of alkali atoms, which does not possess this tunability. As a consequence, one can realize a regime in which the Stark shift and the ponderomotive potential have opposite signs, with the Stark shift dominating over the ponderomotive potential. As such, the use of non-linearly polarized light opens the door for simultaneously trapping atoms away from resonance in a Rydberg state (S -series, P -series, D -series, etc.) and the ground state using Gaussian beams at readily available wavelengths.

III. RESULTS

To start with, we fix the power, beam waist, and wavelength at $P = 2.5$ mW, $w_0 = 1$ μm , and $\lambda = 1,000$ nm, respectively (other wavelengths will be considered later). For these parameters, the Stark shift experienced by the ground state of rubidium is, as can be seen in

Fig. 2(b), negative; the light is red-detuned. The left columns of Figs. 4 and 5 show the total trapping potential $U_{\text{ryd}}(X, 0, Z, \omega)$ for selected rubidium Rydberg states of the $nS_{1/2, +1/2}$ and $nD_{3/2, -3/2}$ series, respectively. In both figures, n is equal to 30, 60, and 80 in the top, middle, and bottom rows, respectively. In Fig. 4, the geometric factor $A \cos \theta_k$ is set to 1 for the $30S_{1/2, +1/2}$ and $60S_{1/2, +1/2}$ states and to 0.3923 for the $80S_{1/2, +1/2}$ state. The resulting potential is positive (indicating anti-trapping) for $n = 30$ but negative (indicating trapping) for $n = 60$ and 80 , with trap depths around a tenth of a milli-Kelvin. The trapping potentials shown in Figs. 4(c) and 4(e) should comfortably hold Rydberg states. In Fig. 5, the geometric factor $A \cos \theta_k$ is set to 1 for the $30D_{3/2, -3/2}$ state, to 0.1915 for the $60D_{3/2, -3/2}$ state, and to 0.0308 for the $80D_{3/2, -3/2}$ state. For the D -states, the resulting potential is negative for all three n considered, with trap depths comparable to those for the $n = 60$ and $n = 80$ S -states.

The ponderomotive potential $U_{\text{pon}}(X, Y, Z, \omega)$ experienced by a Rydberg state is positive for all (X, Y, Z) and wavelengths, provided one works with far off-resonant laser light. As a result, a Rydberg state cannot be confined by a red-detuned optical trap if the only light-induced energy shift is $U_{\text{pon}}(X, Y, Z, \omega)$. However, the Stark shift $U_{\text{stark}}(X, Y, Z, \omega)$ for Rydberg states possesses—as discussed in detail below—an appreciable dependence on $A \cos \theta_k$. This tunability is exploited in Figs. 4 and 5. Specifically, the value of $A \cos \theta_k$ in Figs. 4(e)-4(f) and 5(c)-5(f) are adjusted such that (i) $U_{\text{ryd}}(X, Y, Z, \omega)$ is negative and (ii) the differential potential $\Delta U(X, 0, Z, \omega)$, where $\Delta U(X, 0, Z, \omega)$ is defined through

$$\Delta U(X, Y, Z, \omega) = U_{\text{gr}}(X, Y, Z, \omega) - U_{\text{ryd}}(X, Y, Z, \omega), \quad (8)$$

is minimized. The metric for the minimization is

$$\min \int_{-x_*}^{x_*} \int_{-z_*}^{z_*} |\Delta U(X, 0, Z, \omega)| dX dZ. \quad (9)$$

For the $30S_{1/2, +1/2}$ state considered in Fig. 4(a), a value of $A \cos \theta_k$ that yields a negative $U_{\text{ryd}}(X, Y, Z, \omega)$ was not found. This means that this state cannot be trapped using red-detuned light. For the $60S_{1/2, +1/2}$ state considered in Fig. 4(c) and the $30D_{3/2, -3/2}$ state considered in Fig. 5(a), a value of $A \cos \theta_k = 1$ yields the best result, with $\Delta U(X, 0, Z, \omega)$ being comparable to or just a bit smaller than, in magnitude, the ground state and Rydberg state trapping potentials themselves. For the $80S_{1/2, +1/2}$, $60D_{3/2, -3/2}$, and $80D_{3/2, -3/2}$ states, in contrast, the magnitude of $\Delta U(X, 0, Z, \omega)$ is of the order of a few μK in the regime where the Rydberg atom resides (i.e., inside the region demarcated by the red dashed line), suggesting that the chosen parameters lead to approximately equal trapping potentials for the ground and Rydberg states across the entire Rydberg atom. We can think of this as a magic wavelength-like condition. In

our case, the geometric factor $A \cos \theta_k$ is tuned to realize approximately equal trapping potentials. A change of $A \cos \theta_k$ by about 0.01 for $80S_{1/2,+1/2}$ and $60D_{3/2,-3/2}$ and by about 0.003 for $80D_{3/2,-3/2}$ leads to a change of the metric defined in Eq. (9) by a factor of 2. This shows that the sensitivity of the optimal trapping conditions to the geometric factor depends on the Rydberg state under consideration. While Figs. 4 and 5 are for rubidium, we find analogous magic wavelength-like conditions for cesium (see Appendix B and Figs. 10 and 11).

The discussion above demonstrates that achieving simultaneous trapping of both the ground state and a Rydberg state via a red-detuned laser depends critically on the contribution from the AC Stark shift to the Rydberg potential. In what follows, we provide a detailed analysis of the polarizabilities $\alpha^S(\omega)$, $\alpha^V(\omega)$, and $\alpha^T(\omega)$, and examine how they—together with the geometric factors—enable tuning of the dynamic AC Stark shift and correspondingly of $U_{\text{ryd}}(X, Y, Z, \omega)$. A detailed understanding of the polarizabilities of the Rydberg states for non-linearly polarized light offers valuable insights into how to arrive at optimal trapping conditions for the simultaneous trapping of the ground state and Rydberg states.

Figure 6 shows the scalar, vector, and tensor polarizabilities for selected rubidium Rydberg states as a function of ω . The frequency range shown corresponds to experimentally accessible wavelengths between 500 and 2,200 nm (top axis). Figure 6 considers the $nS_{1/2}$ and $nD_{3/2}$ states with $n = 30$ and $n = 60$. The polarizabilities obtained from the sum-over-states approach are shown by symbols while lines show one-parameter fits (see below) to the numerical data. Note that the tensor polarizability vanishes for the $S_{1/2}$ states due to their spherical shape of the S -orbital. For the $nD_{3/2}$ states with $n = 30$ and $n = 60$, $|\alpha^T(\omega)|$ is smaller than $|\alpha^S(\omega)|$ over the entire frequency range shown. Comparison of the vector and scalar polarizabilities shows the following: For the $30S_{1/2}$ state, $|\alpha^V(\omega)|$ is smaller than $|\alpha^S(\omega)|$. For the $60S_{1/2}$, $30D_{3/2}$, and $60D_{3/2}$ states, in contrast, $|\alpha^V(\omega)|$ is larger than $|\alpha^S(\omega)|$. This suggests that there exists, for each nL_J series, a “reordering” of the polarizability contributions from $|\alpha^V(\omega)| < |\alpha^S(\omega)|$ to $|\alpha^V(\omega)| > |\alpha^S(\omega)|$ as n increases. For the $nD_{3/2}$ series, this reordering occurs for $n < 30$. We confirmed that this reordering exists also for the $nP_{1/2}$, $nP_{3/2}$, and $nD_{5/2}$ series for both rubidium and cesium. The comparatively large magnitude of $\alpha^V(\omega)$ suggests that a positive total polarizability can be realized by tuning $f^V(A, \theta_k, J, M_J)$.

In addition to the relative magnitudes of the contributions to the total polarizability, it is important to comment on the scaling of $\alpha^S(\omega)$, $\alpha^V(\omega)$, and $\alpha^T(\omega)$ with ω . The lines in Fig. 6 show fits of the form $\alpha^S(\omega) = -S\omega^{-2}$, $\alpha^V(\omega) = -V\omega^{-1}$, and $\alpha^T(\omega) = -T\omega^{-2}$ to the numerical data, where S , V , and T are treated as fitting parameters. Figure 6 shows that the single-parameter fits (lines) describe the numerical data (symbols) excellently. This behavior should be contrasted with that for energetically low-lying states. Since the polarizability contributions

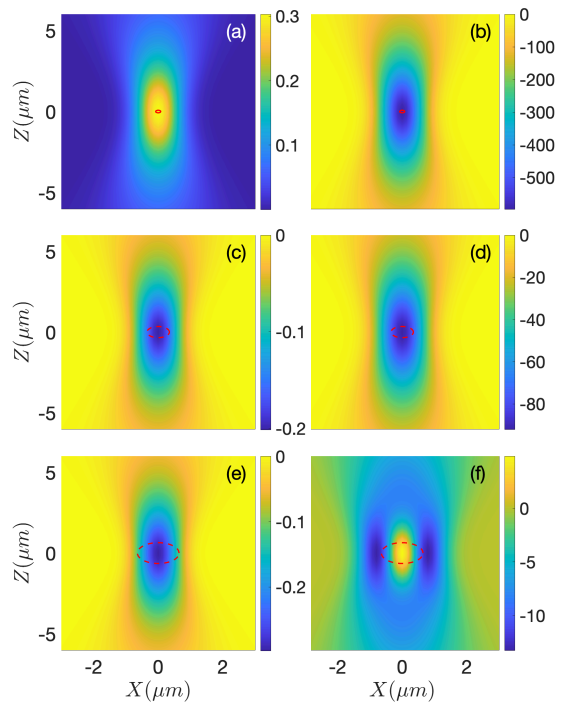


FIG. 4. Trapping of $nS_{1/2,+1/2}$ series of the rubidium Rydberg atom for $\lambda = 1,000$ nm, $w_0 = 1$ μm , $P = 2.5$ mW, and $\theta_p = \pi/2$. Left column: Rydberg trapping potential $U_{\text{ryd}}(X, 0, Z, \omega)$ as functions of X and Z for (a) $n = 30$ and $A \cos \theta_k = 1$, (c) $n = 60$ and $A \cos \theta_k = 1$, and (e) $n = 80$ and $A \cos \theta_k = 0.3923$. The color bars indicate the values of $U_{\text{ryd}}(X, 0, Z, \omega)$ in mK. Right column: Differential trapping potential $\Delta U(X, 0, Z, \omega)$ as functions of X and Z . The n and $A \cos \theta_k$ values in (b), (d), and (f) are the same as those used in (a), (c), and (e), respectively. The color bars indicate the values of $\Delta U(X, 0, Z, \omega)$ in μK (it is important to note that the color bars in the left and right columns use different scales, namely mK and μK , respectively). The red dashed lines demarcate the $(X = x_*, Z = z_*)$ values for which 95 % of the probability of the Rydberg electron, for $Y = 0$, lies inside the red dashed line (see the left column of Fig. 3 for reference).

for the ground state and low-lying excited states tend to feature broad resonances, they do not exhibit a “pure” ω^{-1} or ω^{-2} scaling. By comparison, resonances in Rydberg states are very narrow [40–42]; in fact, Fig. 6 “skips over” them by choosing an ω -grid that excludes various extremely narrow resonances. The fact that the vector and scalar polarizabilities, which have a larger magnitude for Rydberg states than the tensor polarizability, scale differently with ω can be viewed as an “indirect tuning knob” that may be leveraged to find parameter combinations for which the total polarizability of Rydberg states is quite flat over a wide range of frequencies.

To showcase how the frequency-dependent scalar, vector, and tensor polarizabilities change with increasing n , symbols in Fig. 7 show S , V , and T as a function of n for the $nS_{1/2}$ and $nD_{3/2}$ series of rubidium and cesium. It can be seen that the magnitude of S , V , and T increases

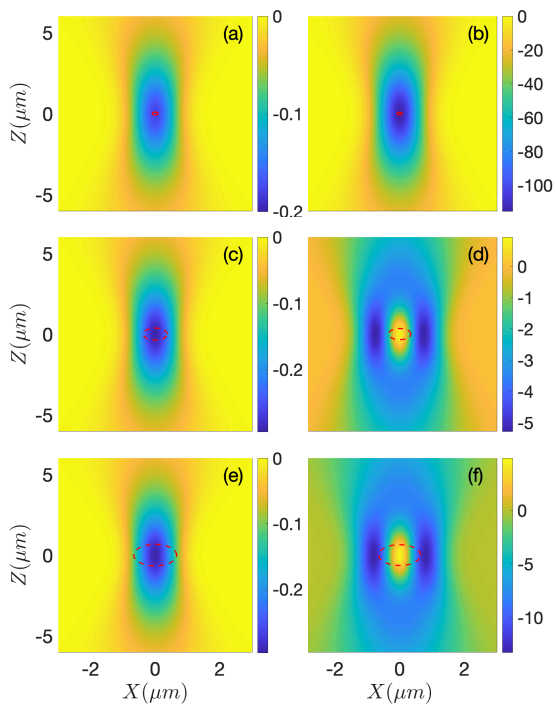


FIG. 5. Trapping of $nD_{3/2,-3/2}$ series of the rubidium Rydberg atom for $\lambda = 1,000$ nm, $w_0 = 1$ μm , $P = 2.5$ mW, and $\theta_p = \pi/2$. Left column: Rydberg trapping potential $U_{\text{ryd}}(X, 0, Z, \omega)$ as functions of X and Z for (a) $n = 30$ and $A \cos \theta_k = 1$, (c) $n = 60$ and $A \cos \theta_k = 0.1915$, and (e) $n = 80$ and $A \cos \theta_k = 0.0308$. The color bars indicate the values of $U_{\text{ryd}}(X, 0, Z, \omega)$ in mK. Right column: Differential trapping potential $\Delta U(X, 0, Z, \omega)$ as functions of X and Z . The n and $A \cos \theta_k$ values in (b), (d), and (f) are the same as those used in (a), (c), and (e), respectively. The color bars indicate the values of $\Delta U(X, 0, Z, \omega)$ in μK (it is important to note that the color bars in the left and right columns use different scales, namely mK and μK , respectively). The red dashed lines demarcate the ($X = x_*$, $Z = z_*$) values for which 95 % of the probability of the Rydberg electron, for $Y = 0$, lies inside the red dashed line (see the right column of Fig. 3 for reference).

monotonically with increasing n . The most prominent feature in Fig. 7 is that the magnitude of V changes by several orders of magnitude as n changes from 30 to 80. Even though the units of V and S differ, it is meaningful to note that the percentage change of $|V|$ with n is larger than the percentage change of $|S|$ with n . This is consistent with the “reordering” of the importance of the scalar and vector polarizabilities discussed in the context of Fig. 6.

We now demonstrate that the vector component affords a tremendous tunability of the total dynamic polarizability $\alpha(\omega)$ for a large number of alkali Rydberg states. Figure 8 depicts $\alpha(\omega)$ for the ground state of rubidium (black dash-dotted line) and the $nS_{1/2,+1/2}$ Rydberg states with (a) $n = 30$ and (b) $n = 60$. The results are shown for the scenario in which the quantization axis is perpendicular to the polarization vector,

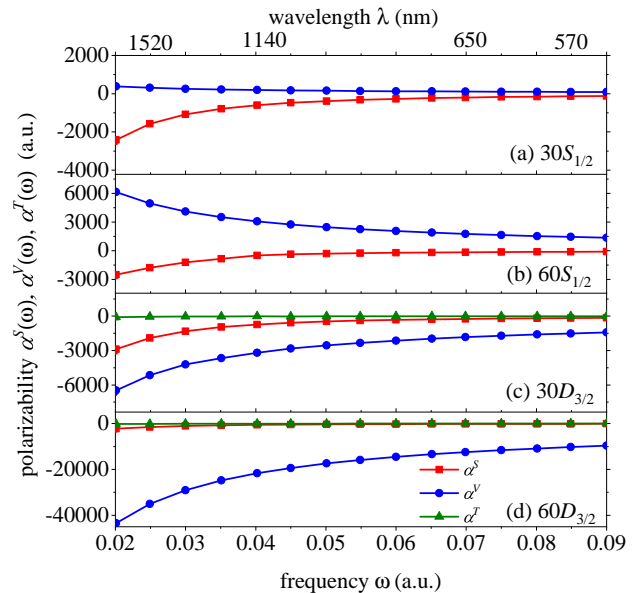


FIG. 6. Squares, circles, and triangles show the numerically obtained scalar, vector, and tensor polarizabilities $\alpha^S(\omega)$, $\alpha^V(\omega)$, and $\alpha^T(\omega)$, respectively, for rubidium as a function of the frequency ω [“a.u.” stands for “atomic unit;” the corresponding wavelengths λ range from 500 nm to 2,200 nm, see the top axis]. The one-parameter fits (lines) agree excellently with the symbols. Panels (a), (b), (c), and (d) are for the $30S_{1/2}$, $60S_{1/2}$, $30D_{3/2}$, and $60D_{3/2}$ states, respectively.

i.e., for $\theta_p = \pi/2$. Since the tensor contribution to the total polarizability is very small, the choice $\theta_p = \pi/2$ provides maximal flexibility in selecting the angle θ_k , which is related to θ_p via the “geometric constraint” $\cos^2 \theta_k + \cos^2 \theta_p \leq 1$ [49, 50]. In Figs. 8(a) and 8(b), the blue dashed line shows the polarizability of the Rydberg state for linearly polarized light ($A = 0$). As expected [40, 41], the Rydberg state polarizabilities are negative for the wavelengths considered. As the polarization of the light changes from linear to elliptical, the polarizability of the Rydberg state with $M_J = +1/2$ shifts up while that with $M_J = -1/2$ shifts down (here, we consider $A \cos \theta_k > 0$; the situation for $A \cos \theta_k < 0$ is reversed). For $n = 30$ [Fig. 8(a)], the shift is very small and lies, for $M_J = +1/2$, between the blue dashed line and the red solid line, which shows the result for the maximal up-shift, namely for $A \cos \theta_k = 1$. For $n = 60$ [Fig. 8(b)], in contrast, the up-shift for $M_J = +1/2$ is appreciable, with the maximal shift occurring for $A \cos \theta_k = 1$ (red solid line). The green lines in-between the blue dashed and red solid lines show the polarizability for various $A \cos \theta_k$. The fact that the total polarizability for $n = 60$ is positive for some geometric factors is a consequence of the reordering of the polarizability contribution from $|\alpha^V(\omega)| < |\alpha^S(\omega)|$ to $|\alpha^V(\omega)| > |\alpha^S(\omega)|$. This observation affords the “counteracting” of the repulsive ponderomotive potential $U_{\text{pon}}(X, Y, Z, \omega)$ by a negative (and larger in magnitude) Stark shift $U_{\text{stark}}(X, Y, Z, \omega)$, as demonstrated in Fig. 4.

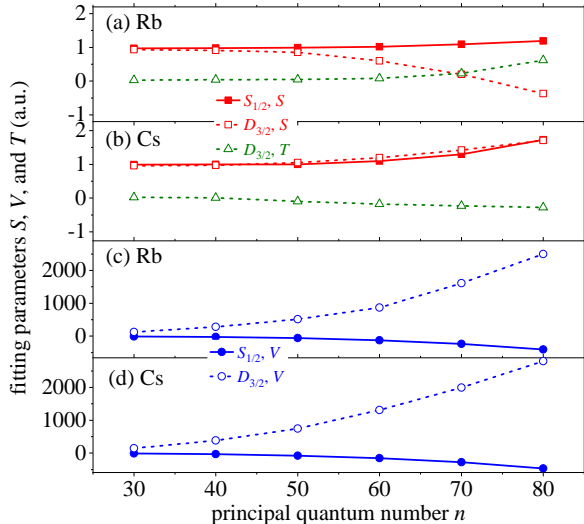


FIG. 7. Symbols in (a)/(b) show the fitting parameters S [$\alpha^S(\omega) = -S\omega^{-2}$] and T [$\alpha^T(\omega) = -T\omega^{-2}$] while symbols in (c)/(d) show V [$\alpha^V(\omega) = -V\omega^{-1}$] as a function of n [to guide the eye, lines connect neighbouring data points]; (a) and (c) are for rubidium while (b) and (d) are for cesium. In (a) and (b), filled squares, open squares, and open triangles show S for the $S_{1/2}$ series, S for the $D_{3/2}$ series, and T for the $D_{3/2}$ series, respectively; in (c) and (d), filled circles and open circles show V for the $S_{1/2}$ and $D_{3/2}$ series, respectively.

Figure 9 shows that the n value for which the vector contribution affords appreciable tunability depends on the Rydberg series considered. While the tunability for the rubidium $nS_{1/2}$ series requires n of order 55, the tunability extends to n values as low as 30. As an example, Fig. 9 shows the $nD_{3/2,-3/2}$ series with $n = 30$ and 60. For this series, the upshift of $\alpha(\omega)$ for $A \cos \theta_k > 0$ occurs for negative M_J , as opposed to for positive M_J as in Fig. 8, since $\alpha^V(\omega)$ is negative. Use of $M_J = +3/2$ would, for $A \cos \theta_k > 0$, lead to a down-shift of $\alpha(\omega)$ of the Rydberg states in Fig. 9. Another notable feature of the tunability via the vector contribution is that the polarizabilities display a relatively weak frequency dependence giving rise to several 100 nm-wide frequency windows in which the ground state and Rydberg state polarizabilities change in a similar manner.

Figure 7 shows that the fitting parameters S , V , and T for the $nS_{1/2}$ and $nD_{3/2}$ series vary roughly in the same manner with n for rubidium and for cesium. This suggests that the tunability afforded by the vector contribution does not only apply to rubidium but also to cesium as well as other alkali Rydberg atoms. Indeed, calculations show that this reasoning is true. As examples, Figs. 13 and 14 from Appendix B show $\alpha(\omega)$ for cesium; the resemblance between the results for cesium and rubidium is evident. Interestingly, though, there exist Rydberg series for which different alkali atoms display distinct behaviors. Figure 15 from Appendix C shows, e.g., that rubidium possesses sufficient tunability to si-

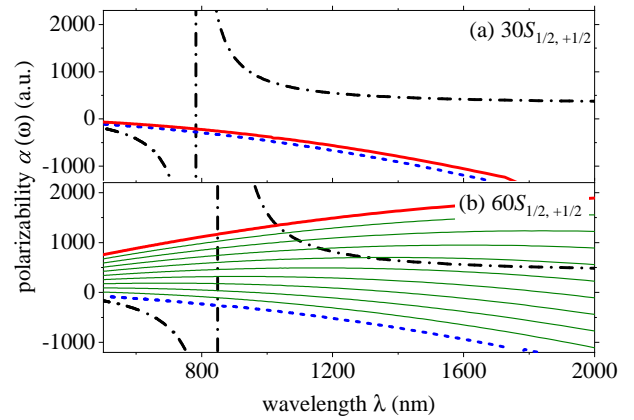


FIG. 8. Polarizability of the ground and Rydberg states for Rb as a function of wavelength. The Rydberg states are (a) $30S_{1/2,+1/2}$ and (b) $60S_{1/2,+1/2}$. The quantization axis is perpendicular to the polarization vector, i.e., $\theta_p = \pi/2$. The black dash-dotted lines show the polarizability of the ground state. The blue dashed and red solid lines show $\alpha(\omega)$ of the Rydberg state for linearly and circularly polarized light, respectively. In (b), the thin green lines show the polarizability of the Rydberg states for elliptically polarized light for various values of $A \cos \theta_k$ [$A \cos \theta_k = 0.1$ (bottom-most curve) to 0.9 (top-most curve)]. For the $60S_{1/2,+1/2}$ state, variation of the geometric factor $A \cos \theta_k$ affords appreciable tunability of $U_{\text{stark}}(X, Y, Z, \omega)$.

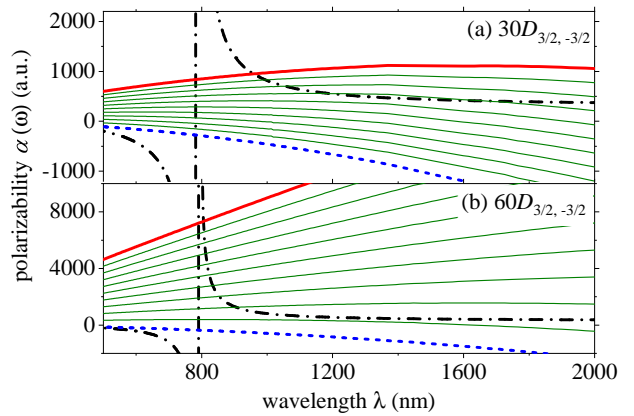


FIG. 9. Same as Fig. 8 but for the $D_{3/2,-3/2}$ states as opposed to $S_{1/2,+1/2}$ states. For both D -states shown, variation of the geometric factor $A \cos \theta_k$ affords appreciable tunability of $U_{\text{stark}}(X, Y, Z, \omega)$.

multaneously trap the ground state and the $60P_{3/2,-3/2}$ Rydberg state, utilizing a positive total polarizability, while cesium does not.

Figures 6-9 illustrate that the Stark shift of the Rydberg atom can be tuned appreciably by tuning the laser wavelength and the geometric factor $A \cos \theta_k$. This tunability is leveraged in Figs. 4, 5, 10, and 11 to engineer the trap potential $U_{\text{ryd}}(X, Y, Z, \omega)$ so as to facilitate the simultaneous trapping of the ground state and a Ryd-

berg state, using parameter combinations that minimize the differential potential $\Delta U(X, Y, Z, \omega)$ for the (X, Y, Z) values where the Rydberg atom has appreciable probability.

IV. CONCLUSION

In conclusion, we propose to employ non-linearly polarized far off-resonant light to exert a force on an alkali Rydberg atom in the direction of the high intensity region of the light by tuning the geometry of the experimental setup (i.e., by varying θ_k and θ_p). The non-linearly polarized light induces a vector polarizability in the Rydberg atom, which is accompanied by a fictitious magnetic field. Working away from resonances, we demonstrated that the vector polarizability cannot only dominate the total polarizability but can also change its sign; for the nS , nP , and nD series investigated, such sign change is not afforded by the scalar and tensor polarizabilities. The resulting Stark shift was shown to “counteract” the repulsive ponderomotive potential, leading to an overall attractive trapping potential. Our approach strongly suppresses unwanted losses, thereby enabling long coher-

To determine the polarizability, we need to determine the eigen states, eigen energies, and dipole matrix elements for the various Rydberg states. Following our earlier work [41], we combine quantum defect theory and the Coulomb approximation method [59, 60]. Since Ref. [41] provided a detailed account of the approach for cesium, including various tables that show excellent agreement with the literature, the discussion here is kept comparatively brief.

According to quantum defect theory, the principal quantum number n and, correspondingly, the energy levels $\epsilon_{n,L,J}$ of single-valence Rydberg states, can be parameterized analogously as those of the hydrogen atom. Specifically, the energy $\epsilon_{n,L,J}$ of a Rydberg state with principal quantum number n , orbital angular momentum quantum number L , and total electronic quantum number J is

$$\epsilon_{n,L,J} = -\frac{m_r \alpha^2 c^2}{2(n_{\text{eff}})^2}, \quad (\text{A1})$$

where m_r denotes the reduced mass of the atom, α the finestructure constant, c the speed of light in vacuum, and n_{eff} the effective principal quantum number. The effective principal quantum number n_{eff} is deduced from the quantum defect parameters $\delta_{L,J,2i}$ by using

$$n_{\text{eff}} = n - \sum_{i=0}^{\infty} \frac{\delta_{L,J,2i}}{(n - \delta_{L,J,0})^{2i}}, \quad (\text{A2})$$

where i is a dummy index. The experimental quantum defect parameters of Rb for the $nS_{1/2}$, $nP_{1/2}$, $nP_{3/2}$,

ence times. Extensions to multiple Rydberg states is an exciting topic for future study.

The proposed approach for trapping Rydberg atoms in the high intensity region of light is expected to enable advances in metrology, such as precision measurements of fundamental constants [12, 51] and Rydberg atom based magnetometry [52], as well as in quantum science, where essentially lossless trapping of Rydberg atoms enables the generation of entangled states [8, 53]. Our proposal may also be applied in Rydberg atom based quantum simulations of spin models, which aim to probe the long time dynamics [53, 54].

V. ACKNOWLEDGMENTS

Fruitful discussions with the Biedermann group are gratefully acknowledged. This work was supported by an award from the W. M. Keck Foundation.

Appendix A: Numerical details and benchmarking

$nD_{3/2}$, and $nD_{5/2}$ states are extracted from Refs. [61, 62] and for $nF_{5/2}$ and $nF_{7/2}$ from Ref. [63]. For Cs, the experimental quantum defect parameters for the $nS_{1/2}$, $nP_{1/2}$, $nP_{3/2}$, and $nD_{5/2}$ states are taken from Ref. [64], for the $nD_{3/2}$ state from Ref [65], and for the $nF_{5/2}$ and $nF_{7/2}$ states from Ref. [66].

Knowing n_{eff} , the wavefunction of a Rydberg state can be approximated using modified Coulomb solutions [67]. This approach has been shown to produce accurate polarizabilities for both Rb and Cs [55, 68]. For Rydberg states, the solution to the radial part of the Schrödinger equation that is regular in the $r \rightarrow \infty$ limit (r denotes the distance of the valence electron from the core) and accounts for the orbital angular momentum barrier and Coulomb potential reads [67]

$$R_{n_{\text{eff}},L,J}(r) = \frac{1}{[a_0 n_{\text{eff}}^2 \Gamma(n_{\text{eff}} + L - 1) \Gamma(n_{\text{eff}} - L)]^{1/2}} \times W_{n_{\text{eff}},L+1/2}(y), \quad (\text{A3})$$

where $W_{n_{\text{eff}},L+1/2}(y)$ with $y = 2r/(n_{\text{eff}}a_0)$ denotes the Whittaker function and a_0 the Bohr radius. The radial wavefunction $R_{n_{\text{eff}},L,J}(r)$ reduces to the well known non-relativistic bound state wavefunction for integer quantum numbers, i.e., for $n_{\text{eff}} = n$ [55]. Using the radial solutions, the radial transition dipole matrix element R_{ki} is given by

$$R_{ki} = \int_{r_0}^{\infty} dr r R_{n_{\text{eff}},k,L_k,J_k}(r) R_{n_{\text{eff}},i,L_i,J_i}(r), \quad (\text{A4})$$

where the lower integration limit r_0 needs to be cho-

TABLE I. The static scalar polarizability $\alpha^S(0)$ and the static tensor polarizability $\alpha^T(0)$ are compared with theoretical and experimental results from the literature (for rubidium, $n = 30, 40, 50, 60, 70,$ and 80 are considered; for cesium, $n = 30$ and 80 are considered). The polarizabilities are reported in atomic units (a.u.) in the format $x[y]$, which stands for $x \times 10^y$ or in the format $x(u)[y]$, which indicates $x \times 10^y$ with uncertainty u in the last digit of x . Entries marked by the superscripts $a, b, c,$ and d are taken from Ref. [55] (theoretical data), Ref. [56] (theoretical data), Ref. [57] (experimental data), and Ref. [58] (experimental data), respectively.

n	scalar polarizability $\alpha^S(0)$					tensor polarizability $\alpha^T(0)$		
	$S_{1/2}$	$P_{1/2}$	$P_{3/2}$	$D_{3/2}$	$D_{5/2}$	$P_{3/2}$	$D_{3/2}$	$D_{5/2}$
Rb								
30	0.555[10]	0.269[11]	0.297[11]	0.101[11]	0.909[10]	-0.277[10]	0.791[10]	0.132[11]
	0.555[10] ^a	0.269[11] ^a	0.297[11] ^a	0.101[11] ^a	0.909[10] ^a	-0.277[10] ^a	0.791[10] ^a	0.132[11] ^a
	0.566[10] ^b	0.275[11] ^b	0.293[11] ^b	0.098[11] ^b	0.916[10] ^b	-0.256[10] ^b	0.824[10] ^b	0.130[11] ^b
	0.559(6)[10] ^d			0.104(4)[11] ^c	0.936(8)[10] ^c		0.784(20)[10] ^c	0.129(4)[11] ^c
40	0.425[11]	0.231[11]	0.256[12]	0.718[11]	0.636[11]	-0.230[11]	0.668[11]	0.111[12]
	0.425[11] ^a	0.231[11] ^a	0.256[12] ^a	0.718[11] ^a	0.636[11] ^a	-0.230[11] ^a	0.668[11] ^a	0.111[12] ^a
	0.438[11] ^b	0.237[11] ^b	0.252[12] ^b	0.695[11] ^b	0.643[11] ^b	-0.210[11] ^b	0.695[11] ^b	0.109[12] ^b
	0.425(8)[11] ^d		0.74(3)[11] ^c	0.67(2)[11] ^c		0.64(3)[11] ^c	0.11(4)[12] ^c	
50	0.203[12]	0.119[13]	0.132[13]	0.329[12]	0.288[12]	-0.116[12]	0.341[12]	0.566[12]
	0.203[12] ^a	0.119[13] ^a	0.132[13] ^a	0.329[12] ^a	0.288[12] ^a	-0.116[12] ^a	0.341[12] ^a	0.566[12] ^a
	0.209[12] ^b	0.122[13] ^b	0.130[13] ^b	0.318[12] ^b	0.291[12] ^b	-0.106[12] ^b	0.356[12] ^b	0.555[12] ^b
	0.203(13)[12] ^d		0.341(12)[12] ^c	0.289(16)[12] ^c		0.329(12)[12] ^c	0.539(20)[12] ^c	
60	0.698[12]	0.455[13]	0.498[13]	0.106[13]	0.106[13]	-0.398[12]	0.132[13]	0.207[13]
	0.747[12] ^b	0.462[13] ^b	0.490[13] ^b	0.110[13] ^b	0.100[13] ^b	-0.393[12] ^b	0.133[13] ^b	0.209[13] ^b
	0.690(3)[12] ^d							
70	0.210[13]	0.135[14]	0.155[14]	0.321[13]	0.285[13]	-0.124[13]	0.397[13]	0.638[13]
	0.219[13] ^b	0.141[14] ^b	0.150[14] ^b	0.316[13] ^b	0.286[13] ^b	-0.118[13] ^b	0.402[13] ^b	0.631[13] ^b
	0.215(8)[13] ^d							
80	0.520[13]	0.364[14]	0.398[14]	0.791[13]	0.709[13]	-0.315[13]	0.101[14]	0.156[14]
	0.550[13] ^b	0.369[14] ^b	0.393[14] ^b	0.788[13] ^b	0.711[13] ^b	-0.306[13] ^b	0.105[14] ^b	0.165[14] ^b
	0.538(52)[13] ^d							
Cs								
30	0.510[10]	0.740[11]	0.968[11]	-0.526[11]	-0.639[11]	-0.865[10]	0.357[11]	0.714[11]
	0.510[10] ^a	0.740[11] ^a	0.968[11] ^a	-0.526[11] ^a	-0.639[11] ^a	-0.865[10] ^a	0.357[11] ^a	0.714[11] ^a
80	0.554[13]	0.119[15]	0.162[15]	-0.821[14]	-0.891[14]	-0.134[14]	0.547[14]	0.976[14]

sen sufficiently small to ensure convergence of the matrix element. We find that $r_0 = \frac{S n_{\text{eff},k} n_{\text{eff},i} a_0}{n_{\text{eff},k} + n_{\text{eff},i}}$ with s around $1/100$ yields converged results. Note that, in terms of the radial wave function $R_{n_{\text{eff}},L,J}(r)$, the wave function $\Psi_{n_{\text{eff}},L,J,M_J}^{(0)}(\vec{r})$ reads $\Psi_{n_{\text{eff}},L,J,M_J}^{(0)}(\vec{r}) = \frac{1}{r} R_{n_{\text{eff}},L,J}(r) Y_{J,M_J}(\hat{r})$ where $Y_{J,M_J}(\hat{r})$ is spherical harmonic of degree J and order M_J .

The total polarizability of an atomic state is composed of the core polarizability, valence-core polarizability, and valence polarizability [32]. The core and valence-core polarizabilities are essentially frequency independent [41] and are calculated using second-order relativistic many-body perturbation theory. The values of the core polarizability for Rb and Cs are 9.08 a.u. and 16.12 a.u., respectively. Since the valence-core polarizability for all Rydberg states considered in the present work is essentially zero, it does not have a contribution to the total polarizability.

To calculate each part of the valence polarizability, i.e., the scalar, vector, and tensor polarizabilities [32, 46, 47],

the sum-over-states method is used [31]. In the sum-over-states method, we include contributions from the virtual excited bound states until convergence is reached. Typically, to obtain converged results for the polarizability of a Rydberg state with principal quantum number n , we include all states that are energetically lower-lying than the Rydberg state of interest and around 50 to 60 states that are energetically higher-lying than the Rydberg state of interest. In all cases, convergence is checked explicitly by increasing the number of states included in the sums.

To benchmark our results, Table I compares the static (i.e., $\omega = 0$) scalar $\alpha^S(0)$ and tensor $\alpha^T(0)$ polarizabilities for rubidium and cesium Rydberg states for selected n values with available theoretical and experimental data from the literature. Our results show good agreement with those of Ref. [55], which employed the same Coulomb approximation method as used in our work. Another recent study [56] calculated the polarizabilities for various rubidium Rydberg states using a model potential and the B-spline expansion technique. The difference between our results and those of Ref. [56] is less

than 5 % across all states considered. Most of our values fall within the experimental uncertainties reported in Refs. [57, 58], with the exception of the scalar polarizabilities for the rubidium $30D_{5/2}$, $40D_{5/2}$, and $60S_{1/2}$ Rydberg states, and the tensor polarizability for the rubidium $50D_{5/2}$ Rydberg state, which deviate by 2σ to 4σ . The overall agreement between our calculations and both theoretical and experimental results demonstrates the reliability of our approach. In addition, we reiterate that our previous work [41] carefully benchmarked the cesium polarizabilities for $n = 40$ – 70 .

Appendix B: Results for cesium

Figures 10 and 11 are analogs of Figs. 2 and 3 of the main text: the main text shows results for rubidium while this appendix presents results for cesium. As in the main text, we use $P = 2.5$ mW, $w_0 = 1$ μm , and $\lambda = 1,000$ nm. For $\lambda = 1,000$ nm, the polarizability of the ground state of Cs is 1075 a.u.. For these parameters, the ground state of cesium experiences a negative Stark shift, allowing for trapping by red-detuned light. The left columns of Figs. 10 and 11 display the total trapping potential $U_{\text{ryd}}(X, 0, Z, \omega)$ for selected cesium Rydberg states in the $nS_{1/2,+1/2}$ and $nD_{3/2,-3/2}$ series, respectively. In Fig. 10, the geometric factor $A \cos \theta_k$ is taken to be 1 for the $30S_{1/2,+1/2}$ and $60S_{1/2,+1/2}$ states, and 0.5352 for the $80S_{1/2,+1/2}$ state. The potential $U_{\text{ryd}}(X, 0, Z, \omega)$ is positive (indicative of anti-trapping) for $n = 30$ but becomes negative (indicative of trapping) for $n = 60$ and $n = 80$. The trapping potentials shown in Figs. 10(c) and 10(e) are expected to be sufficient to trap the corresponding Rydberg states. In Fig. 11, the geometric factor $A \cos \theta_k$ is set to 1 for the $30D_{3/2,-3/2}$ state, to 0.1710 for the $60D_{3/2,-3/2}$ state, and to 0.0919 for the $80D_{3/2,-3/2}$ state. For these D -states, $U_{\text{ryd}}(X, 0, Z, \omega)$ is negative for all three values of n , allowing for trapping of the corresponding Rydberg states.

Similar to what is observed for rubidium, the cesium Rydberg state $30S_{1/2,+1/2}$ shown in Fig. 10(a) cannot be trapped using red-detuned light. In contrast, the cesium states $60S_{1/2,+1/2}$ [Fig. 10(c)] and $30D_{3/2,-3/2}$ [Fig. 11(a)] can be trapped using red-detuned light. For the Rydberg states $80S_{1/2,+1/2}$, $60D_{3/2,-3/2}$, and $80D_{3/2,-3/2}$, the differential potential $\Delta U(X, 0, Z, \omega)$ is on the order of a few μK within the region occupied by the Rydberg atom (as demarcated by the red dashed line in the figures). The, in magnitude, small differential potential indicates that, for the chosen parameters, the trapping potentials experienced by the ground and Rydberg states are nearly identical across the entire extent of the Rydberg electron wavefunction. As discussed previously, we tune $A \cos \theta_k$ to minimize the differential potential, thereby optimizing the trapping conditions. A change of $A \cos \theta_k$ by approximately 0.006, 0.01, and 0.002 for the $80S_{1/2,+1/2}$, $60D_{3/2,-3/2}$, and $80D_{3/2,-3/2}$ states, respectively, results in a change by a factor of 2 in the metric defined in Eq. (9).

Figures 12, 13, and 14 are analogs of Figs. 6, 8, and 9

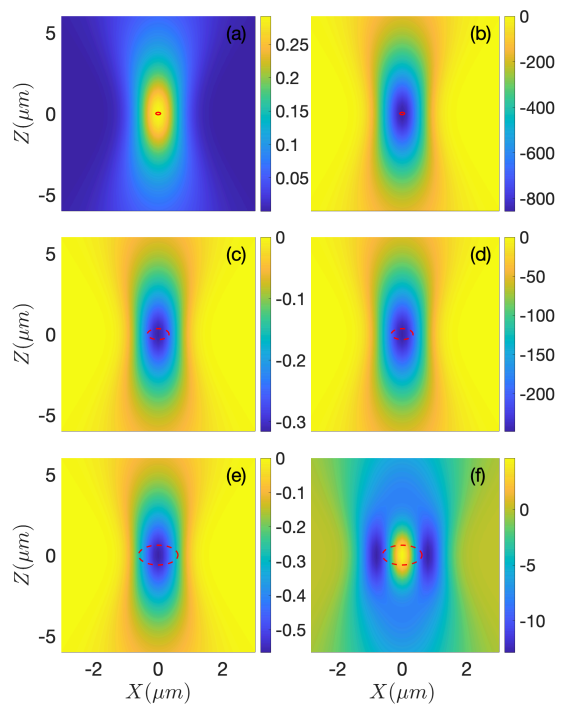


FIG. 10. Trapping of $nS_{1/2,+1/2}$ series of the cesium Rydberg atom for $\lambda = 1,000$ nm, $w_0 = 1$ μm , $P = 2.5$ mW, and $\theta_p = \pi/2$. Left column: Rydberg trapping potential $U_{\text{ryd}}(X, 0, Z, \omega)$ as functions of X and Z for (a) $n = 30$ and $A \cos \theta_k = 1$, (c) $n = 60$ and $A \cos \theta_k = 1$, and (e) $n = 80$ and $A \cos \theta_k = 0.5352$. The color bars indicate the values of $U_{\text{ryd}}(X, 0, Z, \omega)$ in mK. Right column: Differential trapping potential $\Delta U(X, 0, Z, \omega)$ as functions of X and Z . The n and $A \cos \theta_k$ values in (b), (d), and (f) are the same as those used in (a), (c), and (e), respectively. The color bars indicate the values of $\Delta U(X, 0, Z, \omega)$ in μK (it is important to note that the color bars in the left and right columns use different scales, namely mK and μK , respectively). The red dashed lines demarcate the $(X = x_*, Z = z_*)$ values for which 95 % of the probability of the Rydberg electron, for $Y = 0$, lies inside the red dashed line.

of the main text: the main text shows results for rubidium while this appendix presents results for cesium. The key take-away message is that the overall behavior of the polarizabilities of rubidium and cesium Rydberg states is similar for non-linearly polarized light.

Figure 12 presents the scalar, vector, and tensor polarizabilities for the $nS_{1/2}$ and $nD_{3/2}$ Rydberg states ($n = 30$ and $n = 60$) of cesium as a function of ω . It can be seen that for the $30S_{1/2}$ state, $|\alpha^V(\omega)|$ is smaller than $|\alpha^S(\omega)|$. For the $60S_{1/2}$, $30D_{3/2}$, and $60D_{3/2}$ states, in contrast, $|\alpha^V(\omega)|$ is larger than $|\alpha^S(\omega)|$. This behavior is consistent with what is observed for rubidium (see Fig. 6 of the main text). Figure 12 shows that the single-parameter fits (lines) fall essentially on top of the numerical data (symbols), using the fitting functions $\alpha^S(\omega) = -S\omega^{-2}$, $\alpha^V(\omega) = -V\omega^{-1}$, and $\alpha^T(\omega) = -T\omega^{-2}$. The dependence of S , V , and T on n is shown in Fig. 7 of the main

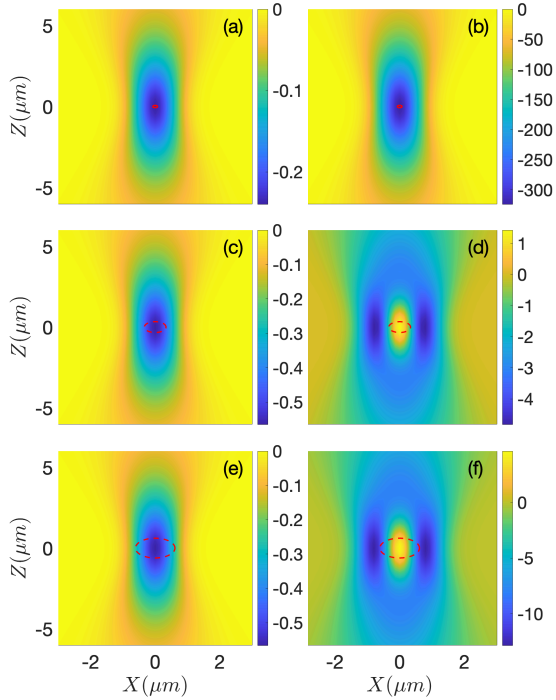


FIG. 11. Trapping of $nD_{3/2,-3/2}$ series of the cesium Rydberg atom for $\lambda = 1,000$ nm, $w_0 = 1$ μm , $P = 2.5$ mW, and $\theta_p = \pi/2$. Left column: Rydberg trapping potential $U_{\text{ryd}}(X, 0, Z, \omega)$ as functions of X and Z for (a) $n = 30$ and $A \cos \theta_k = 1$, (c) $n = 60$ and $A \cos \theta_k = 0.1710$, and (e) $n = 80$ and $A \cos \theta_k = 0.0919$. The color bars indicate the values of $U_{\text{ryd}}(X, 0, Z, \omega)$ in mK. Right column: Differential trapping potential $\Delta U(X, 0, Z, \omega)$ as functions of X and Z . The n and $A \cos \theta_k$ values in (b), (d), and (f) are the same as those used in (a), (c), and (e), respectively. The color bars indicate the values of $\Delta U(X, 0, Z, \omega)$ in μK (it is important to note that the color bars in the left and right columns use different scales, namely mK and μK , respectively). The red dashed lines demarcate the $(X = x_*, Z = z_*)$ values for which 95 % of the probability of the Rydberg electron, for $Y = 0$, lies inside the red dashed line.

text.

Figure 13 depicts the polarizabilities of the ground state (black dash-dotted line) and the $nS_{1/2,+1/2}$ Rydberg state of cesium for (a) $n = 30$ and (b) $n = 60$. The results are obtained, as in Fig. 8 of the main text, for $\theta_p = \pi/2$. The blue dashed and red solid lines show $\alpha(\omega)$ of the Rydberg state for linearly polarized light ($A = 0$) and circularly polarized light ($A \cos \theta_k = 1$), respectively. In Fig. 13(b), the thin green (solid and dotted) lines show the polarizabilities for elliptically polarized light, with the bottom-most curve for $A \cos \theta_k = 1/10$ and the top-most curve for $A \cos \theta_k = 9/10$; these green curves lie between the polarizabilities for linearly and circularly polarized light.

Figure 14 depicts the polarizabilities of the ground

state and the $nD_{3/2,-3/2}$ Rydberg states with $n = 30$ and $n = 60$ of cesium. The presentation is the same as that in

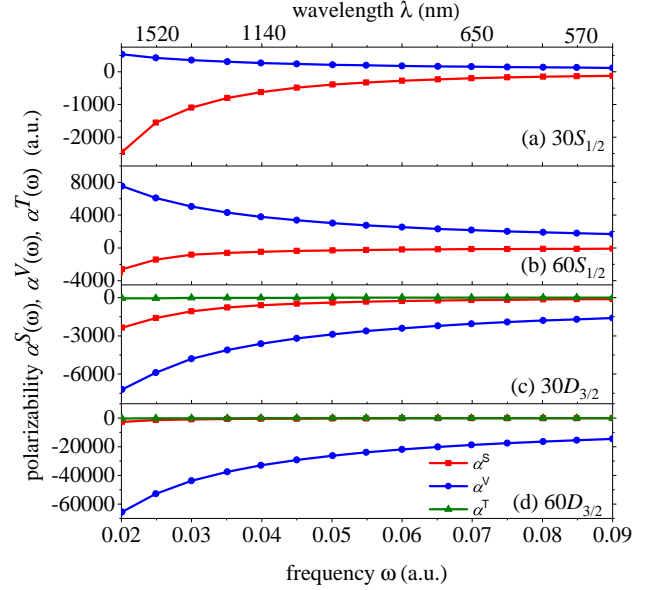


FIG. 12. Squares, circles, and triangles show the numerically obtained scalar, vector, and tensor polarizabilities $\alpha^S(\omega)$, $\alpha^V(\omega)$, and $\alpha^T(\omega)$, respectively, for cesium as a function of the frequency ω [the corresponding wavelengths λ range from 500 nm to 2,200 nm, see the top axis]. The one-parameter fits (lines) agree excellently with the symbols. Panels (a), (b), (c), and (d) are for the $30S_{1/2}$, $60S_{1/2}$, $30D_{3/2}$, and $60D_{3/2}$ states, respectively.

Fig. 13 and Figs. 8 and 9 of the main text. As in the case for rubidium (see Fig. 9 of the main text), we see that $nD_{3/2,-3/2}$ Rydberg states with n as small as 30 feature a positive polarizability if the geometric factor $A \cos \theta_k$ is tuned appropriately. The positive total polarizability is tightly linked to the fact that $|\alpha^V(\omega)| > |\alpha^S(\omega)|$ for the $nD_{3/2,-3/2}$ Rydberg state with $n = 30$.

Appendix C: Comparison of rubidium and cesium

While the qualitative behavior of the polarizabilities of rubidium and cesium is, for many Rydberg states, qualitatively similar, the main text pointed out that this is not always the case. Figure 15 shows an example in support of this discussion. Figures 15(a) and 15(b) show the polarizability of the $60P_{3/2,-3/2}$ state of rubidium and cesium, respectively. One notices the following: (i) $M_J = -3/2$ leads to an upshift for rubidium while $M_J = +3/2$ leads to an upshift for cesium [the ordering of the red solid and red dashed curves in Figs. 15(a) and 15(b) is reversed]. (ii) The maximal shift is much larger for rubidium than for cesium.

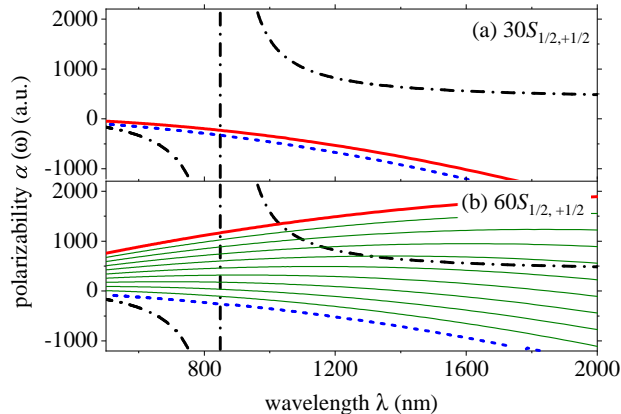


FIG. 13. Polarizability of the ground and Rydberg states for Cs as a function of wavelength. The Rydberg states are (a) $30S_{1/2,+1/2}$ and (b) $60S_{1/2,+1/2}$. The quantization axis is perpendicular to the polarization vector, i.e., $\theta_p = \pi/2$. The black dash-dotted lines show the polarizability of the ground state. The blue dashed and red solid lines show $\alpha(\omega)$ of the Rydberg state for linearly and circularly polarized light, respectively. In (b), the thin green lines show the polarizability of the Rydberg states for elliptically polarized light for various values of $A \cos \theta_k$ [$A \cos \theta_k = 0.1$ (bottom-most curve) to 0.9 (top-most curve)]. For the $60S_{1/2,+1/2}$ state, variation of the geometric factor $A \cos \theta_k$ affords appreciable tunability of $U_{\text{stark}}(X, Y, Z, \omega)$.

-
- [1] M. D. Lukin, Colloquium: Trapping and manipulating photon states in atomic ensembles, *Rev. Mod. Phys.* **75**, 457 (2003).
- [2] T. Peyronel, O. Firstenberg, Q.-Y. Liang, S. Hofferberth, A. V. Gorshkov, T. Pohl, M. D. Lukin, and V. Vuletić, Quantum nonlinear optics with single photons enabled by strongly interacting atoms, *Nature* **488**, 57 (2012).
- [3] O. Firstenberg, C. S. Adams, and S. Hofferberth, Nonlinear quantum optics mediated by Rydberg interactions, *Journal of Physics B: Atomic, Molecular and Optical Physics* **49**, 152003 (2016).
- [4] J. Li, M.-T. Zhou, C.-W. Yang, P.-F. Sun, J.-L. Liu, X.-H. Bao, and J.-W. Pan, Semideterministic entanglement between a single photon and an atomic ensemble, *Phys. Rev. Lett.* **123**, 140504 (2019).
- [5] H. Weimer, M. Müller, I. Lesanovsky, P. Zoller, and H. P. Büchler, A Rydberg quantum simulator, *Nature Physics* **6**, 382 (2010).
- [6] J. Zeiher, J.-y. Choi, A. Rubio-Abadal, T. Pohl, R. van Bijnen, I. Bloch, and C. Gross, Coherent many-body spin dynamics in a long-range interacting ising chain, *Phys. Rev. X* **7**, 041063 (2017).
- [7] D. Malz and J. I. Cirac, Few-body analog quantum simulation with Rydberg-dressed atoms in optical lattices, *PRX Quantum* **4**, 020301 (2023).
- [8] C. S. Adams, J. D. Pritchard, and J. P. Shaffer, Rydberg atom quantum technologies, *Journal of Physics B: Atomic, Molecular and Optical Physics* **53**, 012002 (2019).
- [9] M. Saffman, Quantum computing with atomic qubits and Rydberg interactions: progress and challenges, *Journal of Physics B: Atomic, Molecular and Optical Physics* **49**, 202001 (2016).
- [10] K. C. Cox, D. H. Meyer, F. K. Fatemi, and P. D. Kunz, Quantum-limited atomic receiver in the electrically small regime, *Phys. Rev. Lett.* **121**, 110502 (2018).
- [11] B. Knuffman and G. Raithel, Multipole transitions of Rydberg atoms in modulated ponderomotive potentials, *Phys. Rev. A* **75**, 053401 (2007).
- [12] U. D. Jentschura, P. J. Mohr, J. N. Tan, and B. J. Wundt, Fundamental Constants and Tests of Theory in Rydberg States of Hydrogenlike Ions, *Phys. Rev. Lett.* **100**, 160404 (2008).
- [13] S. Hollerith, J. Zeiher, J. Rui, A. Rubio-Abadal, V. Walther, T. Pohl, D. M. Stamper-Kurn, I. Bloch, and C. Gross, Quantum gas microscopy of Rydberg macrodimers, *Science* **364**, 664 (2019).
- [14] A. Gorlach, O. Neufeld, N. Rivera, O. Cohen, and I. Kaminer, The quantum-optical nature of high harmonic generation, *Nature Communications* **11**, 4598 (2020).
- [15] A. M. Kaufman and K.-K. Ni, Quantum science with optical tweezer arrays of ultracold atoms and molecules, *Nature Physics* **17**, 1324 (2021).

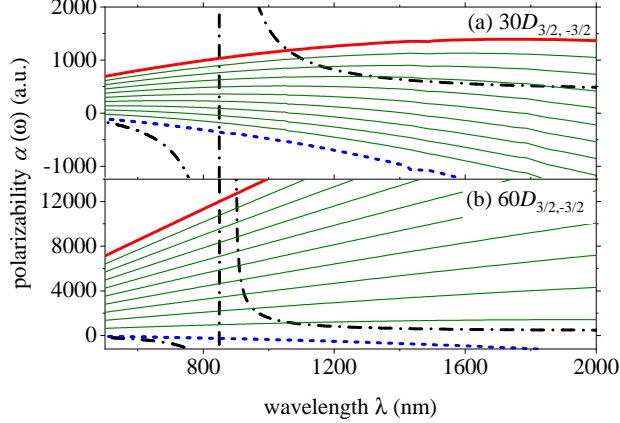


FIG. 14. Polarizability of the ground and Rydberg states for Cs as a function of wavelength. The Rydberg states are (a) $30D_{3/2, -3/2}$ and (b) $60D_{3/2, -3/2}$. The quantization axis is perpendicular to the polarization vector, i.e., $\theta_p = \pi/2$. The black dash-dotted lines show the polarizability of the ground state. The blue dashed and red solid lines show $\alpha(\omega)$ of the Rydberg state for linearly and circularly polarized light, respectively. The thin green lines show the polarizability of the Rydberg states for elliptically polarized light for various values of $A \cos \theta_k$ [$A \cos \theta_k = 0.1$ (bottom-most curve) to 0.9 (top-most curve)]. For both D -states, variation of the geometric factor $A \cos \theta_k$ affords appreciable tunability of $U_{\text{stark}}(X, Y, Z, \omega)$.

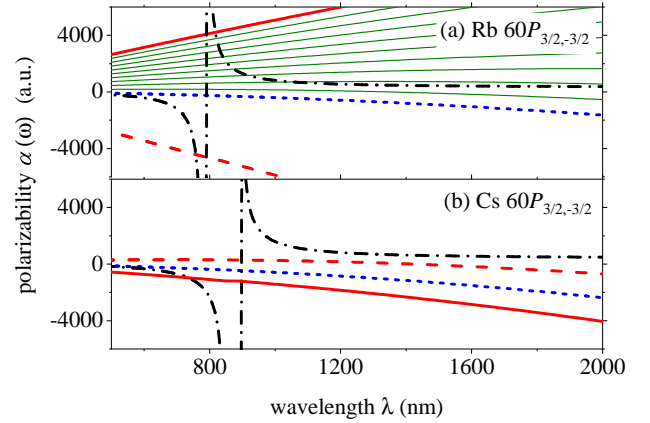


FIG. 15. Polarizability of the ground and Rydberg states for (a) Rb and (b) Cs as a function of wavelength. The Rydberg state is $60P_{3/2, -3/2}$. The quantization axis is perpendicular to the polarization vector, i.e., $\theta_p = \pi/2$. The black dash-dotted lines show the polarizability of the ground state. The blue small-dashed lines show $\alpha(\omega)$ of the Rydberg state for linearly polarized light. Red solid (dashed) lines indicate $\alpha(\omega)$ of the Rydberg state for circularly polarized light with $A \cos \theta_k = +1$ ($A \cos \theta_k = -1$). In (a), the thin green lines show the polarizability of the Rydberg states for elliptically polarized light for various values of $A \cos \theta_k$ [$A \cos \theta_k = 0.1$ (bottom-most curve) to 0.9 (top-most curve)]. For the $60P_{3/2, -3/2}$ state of Rb, variation of the geometric factor $A \cos \theta_k$ affords appreciable tunability of $U_{\text{stark}}(X, Y, Z, \omega)$.

- [16] T.-W. Hsu, W. Zhu, T. Thiele, M. O. Brown, S. B. Papp, A. Agrawal, and C. A. Regal, Single-atom trapping in a metasurface-lens optical tweezer, *PRX Quantum* **3**, 030316 (2022).
- [17] F. Almeida, I. Sousa, O. Kremer, B. P. da Silva, D. S. Tasca, A. Z. Khoury, G. Temporão, and T. Guerreiro, Trapping microparticles in a structured dark focus, *Phys. Rev. Lett.* **131**, 163601 (2023).
- [18] T. Sneh, S. Corsetti, M. Notaros, K. Kikkeri, J. Voldman, and J. Notaros, Optical tweezing of microparticles and cells using silicon-photonics-based optical phased arrays, *Nature Communications* **15**, 8493 (2024).
- [19] V. Shahabadi, E. Madadi, and D. Abdollahpour, Optimized anti-reflection core-shell microspheres for enhanced optical trapping by structured light beams, *Scientific Reports* **11**, 4996 (2021).
- [20] H. Katori, T. Ido, and M. Kuwata-Gonokami, Optimal Design of Dipole Potentials for Efficient Loading of Sr Atoms, *Journal of the Physical Society of Japan* **68**, 2479 (1999).
- [21] J. Ye, H. J. Kimble, and H. Katori, Quantum State Engineering and Precision Metrology Using State-Insensitive Light Traps, *Science* **320**, 1734 (2008).
- [22] L. J. LeBlanc and J. H. Thywissen, Species-specific optical lattices, *Phys. Rev. A* **75**, 053612 (2007).
- [23] A. Cooper, J. P. Covey, I. S. Madjarov, S. G. Porsev, M. S. Safronova, and M. Endres, Alkaline-earth atoms in optical tweezers, *Phys. Rev. X* **8**, 041055 (2018).
- [24] S. Das, A. Bhowmik, K. Mukherjee, and S. Majumder, Transfer of orbital angular momentum superposition from asymmetric Laguerre–Gaussian beam to Bose–Einstein Condensate, *Journal of Physics B: Atomic, Molecular and Optical Physics* **53**, 025302 (2020).
- [25] S. K. Dutta, J. R. Guest, D. Feldbaum, A. Walz-Flannigan, and G. Raithel, Ponderomotive optical lattice for rydberg atoms, *Phys. Rev. Lett.* **85**, 5551 (2000).
- [26] S. Zhang, F. Robicheaux, and M. Saffman, Magic-wavelength optical traps for Rydberg atoms, *Phys. Rev. A* **84**, 043408 (2011).
- [27] T. Topcu and A. Derevianko, Dynamic polarizability of Rydberg atoms: Applicability of the near-free-electron approximation, gauge invariance, and the Dirac sea, *Phys. Rev. A* **88**, 042510 (2013).
- [28] T. Topcu and A. Derevianko, Tune-out wavelengths and landscape-modulated polarizabilities of alkali-metal Rydberg atoms in infrared optical lattices, *Phys. Rev. A* **88**, 053406 (2013).
- [29] D. Barredo, V. Lienhard, P. Scholl, S. de Léséleuc, T. Boulier, A. Browaeys, and T. Lahaye, Three-dimensional trapping of individual Rydberg atoms in ponderomotive bottle beam traps, *Phys. Rev. Lett.* **124**, 023201 (2020).
- [30] N. Manakov, V. Ovsiannikov, and L. Rapoport, Atoms in a laser field, *Physics Reports* **141**, 320 (1986).
- [31] J. Mitroy, M. S. Safronova, and C. W. Clark, Theory and applications of atomic and ionic polarizabilities, *Journal of Physics B: Atomic, Molecular and Optical Physics* **43**, 202001 (2010).

- [32] V. V. Flambaum, V. A. Dzuba, and A. Derevianko, Magic Frequencies for Cesium Primary-Frequency Standard, *Phys. Rev. Lett.* **101**, 220801 (2008).
- [33] J. H. Becher, S. Baier, K. Aikawa, M. Lepers, J.-F. Wyart, O. Dulieu, and F. Ferlaino, Anisotropic polarizability of erbium atoms, *Phys. Rev. A* **97**, 012509 (2018).
- [34] V. V. Tsyganok, D. A. Pershin, E. T. Davletov, V. A. Khlebnikov, and A. V. Akimov, Scalar, tensor, and vector polarizability of Tm atoms in a 532-nm dipole trap, *Phys. Rev. A* **100**, 042502 (2019).
- [35] B. Arora and B. K. Sahoo, State-insensitive trapping of Rb atoms: Linearly versus circularly polarized light, *Phys. Rev. A* **86**, 033416 (2012).
- [36] B. K. Sahoo and B. Arora, Magic wavelengths for trapping the alkali-metal atoms with circularly polarized light, *Phys. Rev. A* **87**, 023402 (2013).
- [37] J. A. Sherman, T. W. Koerber, A. Markhotok, W. Nagourney, and E. N. Fortson, Precision Measurement of Light Shifts in a Single Trapped Ba⁺ Ion, *Phys. Rev. Lett.* **94**, 243001 (2005).
- [38] S. E. Anderson, K. C. Younge, and G. Raithel, Trapping Rydberg atoms in an optical lattice, *Phys. Rev. Lett.* **107**, 263001 (2011).
- [39] J. T. Wilson, S. Saskin, Y. Meng, S. Ma, R. Dilip, A. P. Burgers, and J. D. Thompson, Trapping alkaline earth Rydberg atoms optical tweezer arrays, *Phys. Rev. Lett.* **128**, 033201 (2022).
- [40] J. Bai, S. Liu, J. He, and J. Wang, Towards implementation of a magic optical-dipole trap for confining ground-state and Rydberg-state cesium cold atoms, *Journal of Physics B: Atomic, Molecular and Optical Physics* **53**, 155302 (2020).
- [41] A. Bhowmik, M. Gaudesius, G. Biedermann, and D. Blume, Double, triple, and quadruple magic wavelengths for cesium ground, excited, and Rydberg states, *Phys. Rev. A* **110**, 043114 (2024).
- [42] M. Saffman and T. G. Walker, Analysis of a quantum logic device based on dipole-dipole interactions of optically trapped Rydberg atoms, *Phys. Rev. A* **72**, 022347 (2005).
- [43] L. Li, Y. O. Dudin, and A. Kuzmich, Entanglement between light and an optical atomic excitation, *Nature* **498**, 466 (2013).
- [44] M. Verde, C. T. Schmiegelow, U. Poschinger, and F. Schmidt-Kaler, Trapped atoms in spatially-structured vector light fields, *Scientific Reports* **13**, 21283 (2023).
- [45] A. Bhowmik, N. N. Dutta, and S. Majumder, Tunable magic wavelengths for trapping with focused laguerre-gaussian beams, *Phys. Rev. A* **97**, 022511 (2018).
- [46] A. Bhowmik, N. N. Dutta, and S. Majumder, Vector polarizability of an atomic state induced by a linearly polarized vortex beam: External control of magic, tune-out wavelengths, and heteronuclear spin oscillations, *Phys. Rev. A* **102**, 063116 (2020).
- [47] R.-K. Zhang, J. Jiang, C.-Z. Dong, and Y.-B. Tang, Dynamic polarizabilities and triply magic trapping conditions for $5s^2\ ^1S_0 \rightarrow 5s5p\ ^3P_{0,2}$ transitions of Cd atoms, *Phys. Rev. A* **109**, 032821 (2024).
- [48] J. Lampen, H. Nguyen, L. Li, P. R. Berman, and A. Kuzmich, Long-lived coherence between ground and Rydberg levels in a magic-wavelength lattice, *Phys. Rev. A* **98**, 033411 (2018).
- [49] K. Beloy, *Theory of the ac Stark Effect on the Atomic Hyperfine Structure and Applications to Microwave Atomic Clocks*, Ph.D. thesis, University of Nevada, Reno (2009).
- [50] J. Jiang, L. Jiang, X. Wang, D.-H. Zhang, L.-Y. Xie, and C.-Z. Dong, Magic wavelengths of the Ca⁺ ion for circularly polarized light, *Phys. Rev. A* **96**, 042503 (2017).
- [51] A. Ramos, K. Moore, and G. Raithel, Measuring the Rydberg constant using circular Rydberg atoms in an intensity-modulated optical lattice, *Phys. Rev. A* **96**, 032513 (2017).
- [52] E. K. Dietsche, A. Larrouy, S. Haroche, J. M. Raimond, M. Brune, and S. Gleyzes, High-sensitivity magnetometry with a single atom in a superposition of two circular Rydberg states, *Nature Physics* **15**, 326 (2019).
- [53] X. Wu, X. Liang, Y. Tian, F. Yang, C. Chen, Y.-C. Liu, M. K. Tey, and L. You, A concise review of Rydberg atom based quantum computation and quantum simulation, *Chinese Physics B* **30**, 020305 (2021).
- [54] A. Browaeys and T. Lahaye, Many-body physics with individually controlled Rydberg atoms, *Nature Physics* **16**, 132 (2020).
- [55] V. A. Yerokhin, S. Y. Buhmann, S. Fritzsche, and A. Surzhykov, Electric dipole polarizabilities of Rydberg states of alkali-metal atoms, *Phys. Rev. A* **94**, 032503 (2016).
- [56] Z. Lai, S. Zhang, Q. Gou, and Y. Li, Polarizabilities of rydberg states of rb atoms with n up to 140, *Phys. Rev. A* **98**, 052503 (2018).
- [57] M. S. O'Sullivan and B. P. Stoicheff, Scalar and tensor polarizabilities of ²D Rydberg states in Rb, *Phys. Rev. A* **33**, 1640 (1986).
- [58] M. S. O'Sullivan and B. P. Stoicheff, Scalar polarizabilities and avoided crossings of high Rydberg states in Rb, *Phys. Rev. A* **31**, 2718 (1985).
- [59] M. J. Seaton, Quantum defect theory, *Reports on Progress in Physics* **46**, 167 (1983).
- [60] W. van Wijngaarden and J. Li, Polarizabilities of cesium S, P, D, and F states, *Journal of Quantitative Spectroscopy and Radiative Transfer* **52**, 555 (1994).
- [61] M. Mack, F. Karlewski, H. Hattermann, S. Höckh, F. Jessen, D. Cano, and J. Fortágh, Measurement of absolute transition frequencies of ⁸⁷Rb to nS and nD Rydberg states by means of electromagnetically induced transparency, *Phys. Rev. A* **83**, 052515 (2011).
- [62] W. Li, I. Mourachko, M. W. Noel, and T. F. Gallagher, Millimeter-wave spectroscopy of cold Rb Rydberg atoms in a magneto-optical trap: Quantum defects of the ns, np, and nd series, *Phys. Rev. A* **67**, 052502 (2003).
- [63] J. Han, Y. Jamil, D. V. L. Norum, P. J. Tanner, and T. F. Gallagher, Rb nf quantum defects from millimeter-wave spectroscopy of cold ⁸⁵Rb Rydberg atoms, *Phys. Rev. A* **74**, 054502 (2006).
- [64] J. Deiglmayr, H. Herburger, H. Saßmannshausen, P. Jansen, H. Schmutz, and F. Merkt, Precision measurement of the ionization energy of Cs i, *Phys. Rev. A* **93**, 013424 (2016).
- [65] C.-J. Lorenzen and K. Niemax, Quantum Defects of the $n^2P_{1/2,3/2}$ Levels in ³⁹K I and ⁸⁵Rb I, *Physica Scripta* **27**, 300 (1983).
- [66] J. Bai, R. Song, J. Fan, Y. Jiao, J. Zhao, S. Jia, and G. Raithel, Quantum defects of nF_J levels of Cs Rydberg atoms, *Phys. Rev. A* **108**, 022804 (2023).
- [67] D. R. Bates, A. Damgaard, and H. S. W. Massey, The calculation of the absolute strengths of spectral lines, *Philosophical Transactions of the Royal Society of London. Series A, Mathematical and Physical Sciences* **242**, 101

- (1949).
- [68] W. Van Wijngaarden, Scalar and tensor polarizabilities of low lying S, P, D, F and G states in rubidium, *Journal of Quantitative Spectroscopy and Radiative Transfer* **57**, 275 (1997).